Chemical Engineering Journal Advances 16 (2023) 100525

Contents lists available at ScienceDirect

Chemical Engineering Journal Advances

journal homepage: www.sciencedirect.com/journal/chemical-engineering-journal-advances

Raising the temperature on electrodes for anion exchange membrane electrolysis - activity and stability aspects

T.B. Ferriday [a,b,*], P.H. Middleton [a], M.L. Kolhe [a], J. Van Herle [b]

[a] University of Agder, Department of Engineering Sciences, Jon Lilletuns vei 9, Grimstad, 4879, Agder, Norway
[b] Group of Energy Materials, Swiss Federal Institute of Technology, Lausanne, Rue de l'Industrie 17, Sion, 1951, Valais, Switzerland

ARTICLE INFO

Keywords:
AEM water electrolysis
Heat treating
Cathode
MEA preparation
Hydrogen evolution reaction
AEMWE

ABSTRACT

The membrane electrode assembly is the powerhouse of the anion exchange membrane water electrolyser (AEMWE), thereby placing a great importance on the associated preparation conditions. This paper investigated how annealing temperature and time impacted activity and stability for both anode and cathode electrodes with catalyst-PTFE thin-films. The effect of annealing was thoroughly characterised through SEM/EDS, TEM, XRD, Raman spectroscopy and XPS. Moderate heat-treatment ($T \leq 500°C$) had a positive effect by improving morphology and enhancing reaction kinetics as seen through three-electrode measurements. Annealing temperature affected hydrogen adsorption, resulting in a change in the hydrogen evolution pathway as shown by hydrogen adsorption peaks and Tafel curves. These beneficial effects were further augmented by an enlarged surface area as shown in both three- and two-electrode measurements. Two electrode measurements revealed a staircase activity-trend, where the annealing temperature yielding the greatest activity declined with increasing annealing time. This resulted in efficient cathodes annealed at 2h-500°C, 3h-400°C and 4h-300°C. The aforementioned cell configurations reached approximately 500 mA cm^{-2} at 1.73 V, 1.82 V and 2.04 V respectively. Stable electrodes were produced for temperatures $\leq$500°C, after which their mechanical integrity began to fail due to pyrolysed PTFE. Stability was meticulously characterised and a degradation pathway for carbon catalysts was proposed, where expansion of the carbon black onion layers ultimately lead to catalyst particle detachment.

1. Introduction

The ongoing green-energy shift has greatly accelerated the search for renewable energy technologies which may replace fossil fuel-impelled machinery. Wind energy and photovoltaics are examples of such technology, though efficient energy is necessary for their wide-scale implementation [1–4]. Storing energy in hydrogen by using surplus power to drive electrolysers has proven to be an effective method [1,2], where the emerging technology of anion exchange membrane water electrolysers (AEMWEs) is an exciting option. Through this technology, the benefits of traditional liquid alkaline water electrolysis (AWE) are combined with those of proton exchange membrane water electrolysers (PEMWEs) while simultaneously avoiding their pitfalls [1,3,4]. Specifically, issues of platinum group metal (PGM) dependency associated with PEM technology and the low current densities of traditional AWE are circumvented through AEM electrolysis. This allows the usage of non-PGM catalyst materials while yielding greater current densities than traditionally achieved with AWE [1,3,5,6].

The technology readiness level (TRL) of this technology has yet to reach the level of traditional AWE and PEM technology, and few large scale (>10kW) stacks have been researched and/or produced [7]. As such, the research interest in AEM electrolysis has drastically increased and the number of papers published on the topic shows an exponential growth. All aspects of AEM electrolysis are currently being investigated to advance the TRL, the most paramount of which includes preparing stable and active membrane electrode assemblies (MEAs), scaling issues and balance of plant. The MEA comprises the anode micro-porous layer (MPL), the anode catalyst layer (CL), the polymeric membrane, the cathode CL and the cathode MPL. This facet is arguably the most important part of the electrolytic cell as it facilitates transportation of both reactant/product and hosts the three-phase interface, home to all electrochemical reactions [3].

Typical components in MEAs include ionomers which facilitate ion transportation in the three-phase boundary layer and various types of binder which will aid the ionomer in providing mechanical integrity to the MEA while also improving mixed-phase fluid dynamics. Faid et al.

* Corresponding author.
E-mail address: thomasbferriday@gmail.com (T.B. Ferriday).

https://doi.org/10.1016/j.ceja.2023.100525
Received 21 April 2023; Received in revised form 10 June 2023; Accepted 16 June 2023
Available online 23 June 2023

[8] revealed that the cathodic sensitivity to ionomer content was significantly greater than that of the anode. The ideal loading of the Fumion® anion exchange ionomer (AEI) was determined to be 10 wt.% of the coated catalyst for that specific nickel-based electrode. Moreover, catalyst coated substrates (CCSs) composed of both the Fumion® AEI and the Nafion® ionomer were created and compared. Linear sweep voltammetry (LSV) and electrochemical impedance spectroscopy (EIS) measured on a rotating disc electrode displayed that the thin films containing the Nafion® ionomer outperformed the Fumion® AEI with both Ni/C and NiO catalysts. Moreover, in-situ half-cell tests revealed the consequences of replacing a PGM anode/cathode with a non-PGM alternative. The reduced efficiency through the replacement of the PGM cathode was significantly higher than that using a non-PGM anode catalyst, thereby displaying the remaining dependency of a Pt cathode [6,9].

MEA preparation methods have also received attention where the effect of hot-pressing anodes with varying PTFE binder content was investigated by Cho et al. [10]. The greatest performance was achieved using 9 wt.% PTFE which was confirmed in work by Ito et al. [11] for both anodes and cathodes. While the usage of hot-pressing in association with AEMs is debated due to adverse effects on the polymeric membrane [1,3], the aforementioned publication reported positive effects from hot-pressing up to 50°C, including an enhanced ionic conductivity and an augmented electrochemical surface area. Adding PTFE to Nafion® has been reported to increase its thermal stability [12], thus PTFE can have a stabilising effect against heat treatment of either a CCS or a catalyst coated membrane (CCM) in addition to adding alkaline stability [13,14].

PTFE has hydrophobic qualities which will improve mass transportation by increasing the rate of bubble detachment in the three-phase interface [3,10]. However, PTFE is also a natural insulator and will increase series resistance, meaning the optimal PTFE quantity is ultimately a trade-off between improved fluid dynamics and restricted charge transfer [10].

Improved stability and activity has been reported for electrodes annealed at 200°C for 30 min [15,16], however optimised conditions for such treatment have yet to be reported for AEM water electrolysis. While the practice of heat-treating catalyst powders is widespread [6], the same treatment is rarely reported for CCSs in part due to the material stability of the ionomer. The addition of PTFE in the thin-film can aid in increasing the thermal stability, and by that enable the use of heat treatments. High-temperature treatment has resulted in smaller particle sizes [17,18], improved morphologies [16,19,20] and overall increased catalytic activity [16].

This paper will explore how electrode annealing conditions, namely temperature and duration, impact electrode performance and stability in an anion exchange membrane water electrolyser. Both the anode and cathode were investigated where a PGM cathode catalyst was utilised to emphasise activity and stability [10]. The Pt/C on nickel foam substrates were heat treated in an argon atmosphere at temperatures between 300–600°C for 2–4 h. The electrodes were tested in a standard three-electrode setup and in a single-cell AEMWE.

The addition of PTFE in the catalyst ink increased thermal stability, however at the cost of increasing the series resistance. This series resistance was halved when the temperature was increased to 500°C and 600°C when heat treated for 2 h.

Longer heating durations yielded decreasing performances. The greatest activity temperature ($T_{act.,\ max}$) decreased with increasing heating time. The greatest AEMWE performance was achieved utilising the 2h-500°C cathode, yielding 1000 mA cm^{-2} at 1.86 V with iR-correction. Stability was quantified through a series of physicochemical tests, revealing that excessive temperatures (T> 500°C) exacerbated surface carbon degradation, causing catalyst detachment. The addition of PTFE increased stability, as seen by the greater stability of cathodes heat-treated at 300–400°C compared against the electrodes annealed at 600°C, where PTFE was no longer present. Extended activation through chronopotentiometry in a kinetically controlled region, herein termed kinetic conditioning yielded performance improvements for all 12 cell configurations.

2. Experimental

2.1. Chemicals

The anode $NiFe_2O_4$ catalyst was purchased from US Research Nanomaterials, the cathode 20 wt.% Pt/C catalyst was procured from the online store fuelcellstore.com and the polytetrafluoroethylene preparation 60 wt.% dispersion in H_2O was bought from Sigma Aldrich together with the 5 wt.% Nafion® perfluorinated resin solution. The Sustainion® X37-50 AEM was purchased from DiOxide Materials.

2.2. Membrane electrode assembly preparation

The membrane electrode assembly (MEA) was created and utilised according to the illustration given in Fig. 1. All substrates were initially reduced in thickness to approximately 0.4 mm by hammering. The MEA was composed of a $NiFe_2O_4$ anode, a Sustainion® X37-50 anionic exchange membrane and a Pt/C cathode. The anode ink was prepared by dispersing $NiFe_2O_4$ in deionised water and isopropanol (0.5/0.5 vol.%) and mixing in 20 wt.% of 5 wt.% Nafion® perfluorinated resin solution and 10 wt.% of polytetrafluoroethylene preparation 60 wt.% dispersion in H_2O to ensure sufficient binding and an appropriate degree of hydrophobicity in the catalyst layer. The ink was ultra-sonicated for 15 min before spray coating over a 3.3x3.3 cm nickel foam substrate attached to a metal plate heated to approximately 80°C (Fig. S1a). The resulting catalyst loading was approximately ~5 $mg_{NiFe_2O_4}$ cm^{-2}. The anodes were subsequently heat treated at 400°C for 2 h in an argon atmosphere utilising a Carbolite tube furnace.

A sheet of Sustainion® X37-50 was stored in 1.0M KOH at room temperature for at least 24 h for activation before appropriately sized membranes were cut. The total active area of the membrane was 10 cm^2.

The cathode catalyst ink comprised the same ingredients as the anode ink, with 20 wt.% Pt/C in place of the spinel anode catalyst. The cathode ink was spray coated on nickel foam substrates through the same procedure as detailed with the anode. A very low platinum loading of ~ 0.2 mg_{Pt} cm^{-2} was utilised in the cathodes. A total of 12 cathodes were heat treated under different conditions, varying between 300, 400, 500 and 600°C for 2, 3 and 4 h.

2.3. Spectroscopic characterisation

The morphology of the electrodes was analysed in a Jeol JSM-7200F field emission scanning electron microscope (SEM). Electrodes were analysed after heat treatment and after electrochemical testing to determine any changes in general morphology or surface conditions. The centres and edges of the electrode were also analysed to ensure uniformity of the catalyst layer. Moreover, elemental mapping was performed through energy dispersive spectroscopy (EDS), thereby allowing bulk quantification of each element.

X-ray photoelectron spectroscopy (XPS) was carried out using a Kratos AXIS Supra with an Al Kα X-ray monochromatic source (hν=1486.6 eV at 10 A and 15 kV). The survey and high-resolution spectra were collected employing step sizes of 1 eV and 0.1 eV respectively. Similarly, the pass-energies were 160 eV for survey spectra and 40 eV for the high-resolution core-level spectra. Analysis of the spectra was conducted using CasaXPS software, while the binding energy axis was calibrated using the photoemission peak affiliated with C 1s adventitious carbon (C–C) located at 284.8 eV.

X-ray diffraction (XRD) was performed with a Bruker D8 Advance where all Bragg Brentano measurements were in reflection mode. The X-

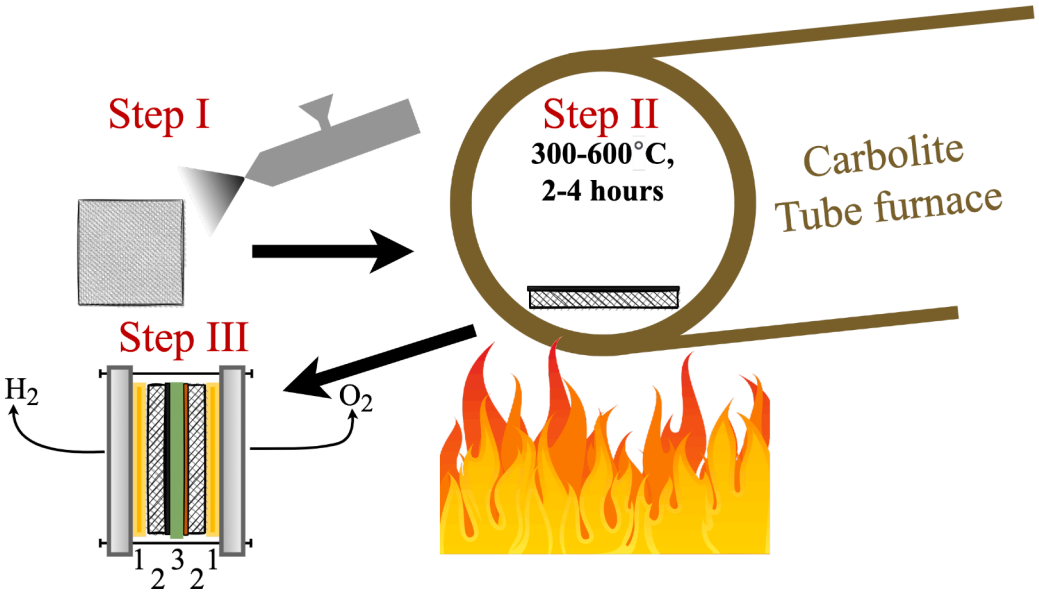

Fig. 1. Visualised experimental methodology. **Step I**: The nickel foam substrates were spray coated with either a Pt-ink (black) for the cathode or a $NiFe_2O_4$-ink (brown) for the anode. **Step II**: The cathodes were annealed in an inert argon atmosphere at temperatures of 300-600°C for 2 to 4 h. The anodes were heated at 400°C for 2 h. **Step III**: These electrodes were utilised in an AEMWE, shown with the current collectors (1), anode/cathode electrodes (2) and the anion exchange membrane (3).

ray source was a Cu kα (1.5406 Å), operated at 40 kV, 40 mA (1600 W). The thin-films were measured while on the nickel foam support, alas the nickel adds a notable contribution due to its great volume compared against the thin-film. Thus, the diffraction peaks associated with the nickel foam were neglected in the analysis of the Pt/C cathodes.

A Raman InVIa Renishaw was used for Raman spectroscopy with a 100x lens, where the spectra were obtained by excitation with a He-Ne laser with a wavelength of 632 nm. The built-in cosmetic function was selected, implying each scan was repeated three times allowing stray peaks to be filtered out. Raman data processing and fitting was executed with the protocol established for carbon black materials [21–26] using the open-access software Fityk [24,26]. The I_D/I_G ratios were determined based on integrating the associated peaks [24].

2.4. Electrochemical characterisation

Electrochemical characterisation was performed using an Iviumstat electrochemical workstation. An efficient three-electrode setup was utilised to analyse the anode/cathode separately, with a Ag/AgCl-reference electrode (KCl = 3.0 M) (Metrohm) and a platinum counter electrode similar to our previous works [27–29]. The electrodes employed in this setup were all 1 cm^2.

For cathodic three-electrode measurements, electrochemical impedance spectroscopy (EIS) spectra were collected between 1×10^5 and 4×10^{-1} Hz with 15 points per decade and an AC sinusoidal pulse amplitude of 6 mV. EIS spectra were recorded at open circuit in addition to potential offsets of -50 mV_{RHE} and -100 mV_{RHE}. Linear sweep voltammetry (LSV) curves were registered between from 0.30 down to -0.20 V_{RHE} at 2 mV s^{-1}, from which Tafel slopes and exchange current densities were estimated through the Tafel approximation [30]. Cyclic voltammetry (CV) was performed between 0.6-0.7 V_{RHE} at 10:2:20 mV s^{-1} to determine the double layer capacitance (C_{dl}), and subsequently between -0.05-1.4 V_{RHE} at 50:50:300 mV s^{-1} to probe the electrode for redox couples and determine the electrochemical activity. The same sequence of experiments was performed for the anode, although with different potentials. Specifically, EIS spectra were collected at open circuit in addition to potential offsets of 1.5 V_{RHE}, 1.55 V_{RHE}, 1.60 V_{RHE} and 1.65 V_{RHE}. LSV curves were registered between 1.30-1.70 V_{RHE} at 2 mV s^{-1}. Cyclic voltammograms were collected between 0.986-1.086 V_{RHE} at 10:2:20 mV to ascertain C_{dl} and between 0-1.60 V_{RHE} to measure redox couples and their degree of activity.

A two-electrode setup utilising 10 cm^2 electrodes was employed for whole-cell measurements (Fig. S1b). For two-electrode measurements, EIS spectra were collected between 10^5 and 10^{-1} Hz with 10-15 points per decade and an AC sinusoidal pulse amplitude of 10 mV. Spectra were collected at open circuit and with potential offsets of 1.50, 1.60, and 1.70V. LSV was measured between 0 and 2.50 V with a sweep rate of 25 mV s^{-1} and a 5.0 mV step. Cyclic voltammetry (CV) was measured between 0 and 1.40 V_{RHE} at 50, 100, 200, 300, 400 and 500 mV s^{-1}.

The cells were tested several times to gain information on how the performance of each cell configuration varied after rest and after an extended activation period. The cell was operated under kinetic control (50 mA cm^{-2}) for five hours, herein termed kinetic conditioning. The alkaline electrolyte was initially pumped through the cell while its temperature slowly increased towards 50°C using cartridge heaters fixed into the endplates of the cell as seen in Fig. S1b. Several EIS spectra were collected at open circuit potential throughout the approximately 30-min heating process to check for short circuits. The cell was assumed to be stable if it continued to show the same behaviour throughout the heating process, allowing the testing protocol to commence.

EIS spectra were initially collected at open circuit potential, followed by LSV to determine the initial performance. Chronoamperometry (CA) was performed at 1.70 V over 10 min, or until a stable current was achieved to aid in ensuring steady state measurements. Open circuit EIS spectra were collected again followed by LSV. Whole-cell EIS spectra were then measured while the cell was polarised at 1.50 V, 1.60 V and 1.70 V. Cyclic voltammograms were collected, where all measurements were repeated until a steady state response was obtained, where this was indicated by overlapping scans. The cell was then allowed to cool down to room temperature and rest for 24 h. The pumps were turned off once the cell had returned to an ambient temperature, thereby allowing the cell to rest and thereby simulate the intermittent use faced by electrolysis systems connected to renewable energy systems [2].

Day two of testing was elicited by heating the cell while flowing the electrolyte and activating the cell again through 10 min of CA at 1.70 V, or until a stable current was recorded. Following the same protocol as day 1, open circuit EIS was then collected, followed by LSV, CVs and polarised EIS. Kinetic conditioning was performed at 50 mA cm^{-2} for five hours, where this duration and current density was chosen, as the greatest loss of performance usually occurs during the first few hours of a stability test [31–33], and this current density ensures the electrolysis cell is working the region controlled by activation overpotential. Open circuit EIS, LSV, CVs and polarised EIS spectra were all collected again to quantify the state of the cell following the five hours of CP. Degradation

rates were determined by measuring the potential difference between a stable initial potential and the final potential, where all related details are listed in Tab S1. All cell configurations were subjected to these tests in the same order. Ohmic compensation of LSV curves was performed employing the first x-axis intercept of the polarised EIS spectra, commonly referred to as the series resistance, R_s [5,34]. Untreated nickel foam was utilised as a reference and will serve as a basis for comparison against the annealed electrodes.

3. Results and discussion

3.1. Spectroscopic

The SEM images in Fig. 2a–d show the platinum-PTFE cathodes after annealing at 300, 400, 500 and 600°C for 4 h. Electrode morphology changes as the temperature increases, where the underlying nickel foam structure becomes increasingly visible as shown by comparing the aforementioned figures to the reference nickel foam shown in Fig. 2e and Fig. S2. A clear change is also seen in the atomic composition of the electrodes, where the atomic percentage of fluorine declines rapidly at 600°C which indicates that both the Nafion resin and the PTFE have been affected by the temperature and likely been pyrolysed as shown by Fig. S3a-S3b. The decline in fluorine and the notable reduction in wt.% (Fig. S3c) at 600°C explains the changes in morphology seen in the SEM images below and correlated with established literature [35]. Fig. 2a–c display a continuous thin-film covering the majority of the recesses in the nickel foam structure, which is not the case in Fig. 2d as the excessive temperature has pyrolysed the thin film, leaving the only the Pt/C catalyst and some remnants of the PTFE binder. No time-related changes in morphology were noted.

It has been documented that thin-film cracks have accompanied the usage of IPA as a solvent [36], however SEM figures of pre-heat-treated thin films shown in Fig. S3 display that this is not the cause of the cracks in the present case. Thermal expansion of nickel could have an impact, as it is predicted to expand corresponding to an increased circumference of 2.83–6.27 μm based off a thermal expansion coefficient in the region of 16.24–17.36 m m^{-1} K^{-1} [37] and perfectly circular nickel strands. While this expansion only amounts to ≈0.5-1.0% of the total circumference, it is still likely to add some additional strain on the thin-film.

The EDS mapping in Fig. 2f displays that all elements are homogeneously distributed in the thin-film. Moreover, EDS data in Fig. S5-S7 also shows that sulphur is still present in the thin-film after heat treatment up to 500°C and only weakly so at 600°C. The only source of this element in the thin-film is the sulphonic group of the Nafion perfluorinated resin solution. The stability of Nafion in H^+-form is limited by the thermal stability of the sulphonic group, i.e. the source of sulphur.

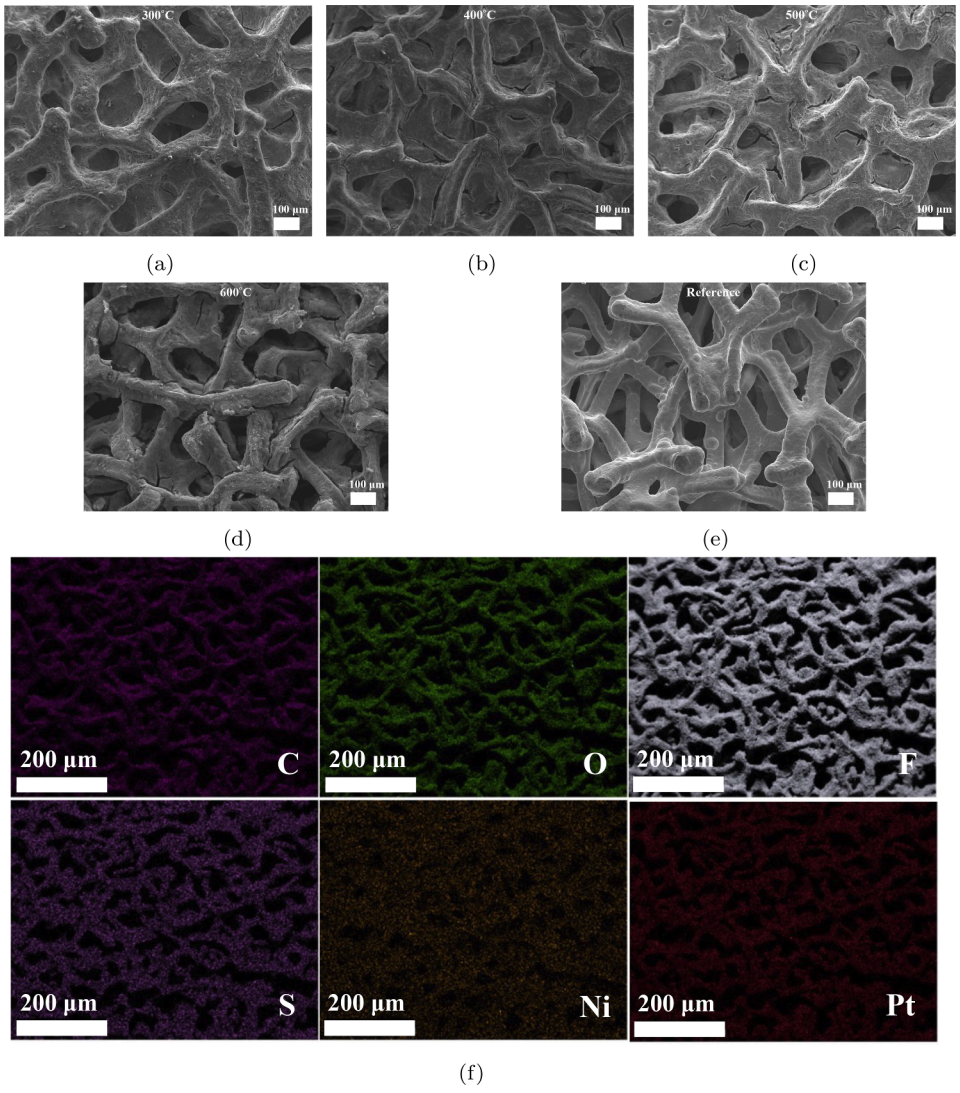

Fig. 2. Scanning electron microscope (SEM) images of the Pt-PTFE electrodes after 4 h of annealing at **(a)** 300°C, **(b)** 400°C, **(c)** 500°C, **(d)** 600°C and **(e)** a reference piece of nickel foam. **(f)** EDS mapping of the Pt-PTFE electrode heat treated at 300°C for 4 h.

A complete absence of these groups was noted through thermal gravimetric analysis at 280°C in a 5%H_2/95%N_2 atmosphere [38,39] and 300°C based on infrared reflectance absorption spectroscopy [40]. However, impregnation of Nafion into PTFE has been shown to increase the thermal stability of Nafion [12]. While no direct impregnation of Nafion into PTFE was facilitated in the creation of these thin-films, it is still likely that surface PTFE will serve as a protective layer for the Nafion resin in the bulk of the porous thin film. There are several sulphur-based degradation products of Nafion, however these are predominantly gaseous and thereby unlikely to remain in the film after heat-treatment [12,39,40]. SEM/EDS analysis has shown the annealing process has produced catalyst thin-films with uniform composition and a rather smooth surface which critically cracks when the temperature exceeds 500°C.

Anode SEM results in Fig. S9a present a more rugged surface, and EDS mapping and quantification in Fig. S9b-S9c indicate a slightly less uniform dispersion of the catalyst elements.

TEM imaging was employed to analyse the Pt-PTFE surfaces on a nano-scale, where bright-field TEM images in Fig. 3a–c show the state of the thin-film in pristine condition after annealing. Fig. 3a & b show circular Vulcan XC-72 support particles bejewelled with platinum nanoparticles. The change with temperature is illustrated in Fig. 3a and c, where the first two images show defined carbon particles (grey and light-grey), whereas the 600°C sample in Fig. 3c displays greater disorder and less defined particles. Generally, the platinum nanoparticles appear evenly distributed over the support with little influence of agglomeration, a condition which does not change with temperature. STEM figures in Fig. 3d show presence of oxygen, platinum and fluorine, where the size of the platinum nanoparticles varied between 1-2 nm.

The state of the catalyst is further analysed with HRTEM, where the classic onion-like carbon support structure is shown in Fig. 3e and f, over which the Pt-particles are evenly distributed. The in-plane distance of carbon was measured to 3.39 Å with a standard deviation of 0.34 Å as shown in the in-plane size distribution in Fig. S10d which corresponds to the d_{002} plane of graphitic carbon [26,41]. The in-plane Pt-Pt distance was also measured to 2.24 Å (std = 0.15 Å) which is affiliated with the d_{111} spacing [41].

XRD was gathered to investigate the crystallographic nature of the Pt-PTFE electrodes. Fig. 4a shows XRD patterns of a pristine and a heat-treated Pt/C cathode. Diffraction peaks at Bragg angles of $2\theta = 17.1°$, 18.2° and 40.06° are observed. Only minor variations in peak position in the range of 0.01° were noted, where this originates most likely from height variations during sample mounting due to the fragile nature of the electrodes. The peaks at 17.1° and 18.2° are related to the Nafion resin and Nafion + PTFE respectively (JCPDS No. 47-2217) [16,42–44]. The large peak width and low intensity of the Nafion peak at 17.1° corresponds to the amorphous nature of the ionomer structure. This peak is not visible in the untreated sample, which indicates a clear increase in crystallinity after annealing. The clear PTFE peak at 18.2° is due to the crystalline nature of PTFE [16,42]. The peak at 40.06° was attributed to the platinum facet (111) [16,45]. The pristine sample shows a very amorphous Pt (111) peak, whereas the crystallinity was enhanced after annealing. Curiously, the amorphous peak related to the carbon support around 25° [16,42,43] was not conclusively observed in either spectra, however this could be due to the XRD-scanning conditions. Additional XRD spectra in Fig. S11 shows similar changes to those seen in EDS data, where the peak corresponding to PTFE+Nafion at 18.2° declines with increasing temperature and disappears completely at 600°C. This influence of heating was also observed between the unheated and the heated samples in Fig. 4a.

The anode XRD spectra in Fig. S12 displays peaks at $2\theta = 18.1°$, 30.5°, 35.6°, 37.5°, 43.5°, 53.8°, 57.5° and 63.1°. Similarly to the cathodes, the initial peak at 18.12° is due to the Nafion resin + PTFE [16,42,44]. The remaining peaks originate from the (220), (311), (222), (331), (422), (511) and (440) planes of $NiFe_2O_4$ (JCPDS No. 10-0325) [46]. Additional peaks are also seen at 44.54° and 54.90°, though these are attributed to the 111 and 200 planes in the nickel foam support (JCPDS No. 87-0712) [47]. The singular peak around 17° corresponding to the Nafion resin was not conclusively observed on the anode, however its diffuse nature renders visibility poor. Comparing the XRD spectra

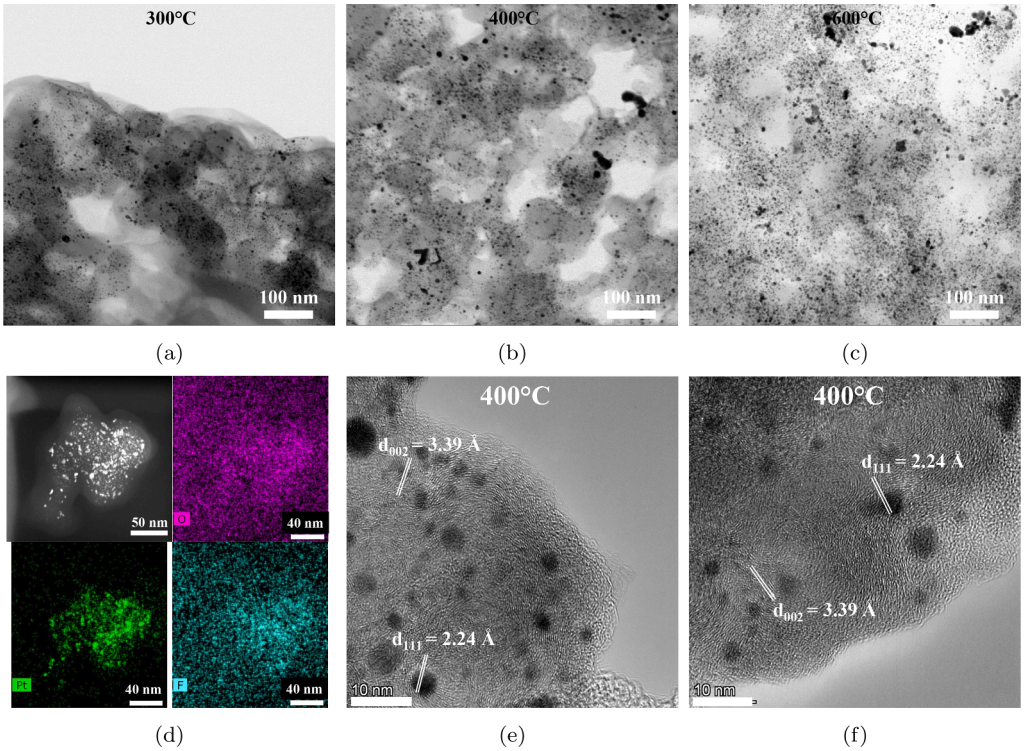

Fig. 3. Part **(a)**–**(c)** displays bright field TEM images of the cathode heated for 2h-300°C, 2h-400°C and 2h-600°C. **(d)** STEM images of a cluster of Pt/C nanoparticles. HRTEM in (e) and (f) show structure of carbon structure and platinum particles.

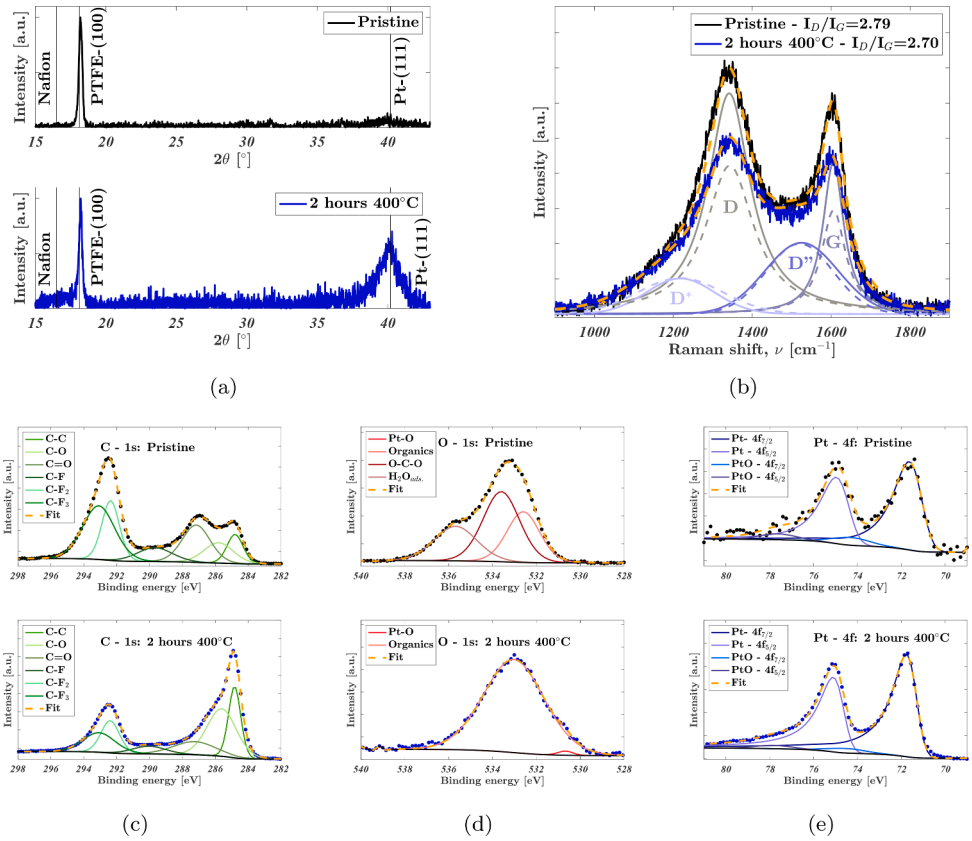

Fig. 4. Surface analysis of the Pt/C electrodes were conducted before and after annealing (2 h, 400°C), with XRD spectra **(a)** and **(b)** Raman spectra. Annealed fitting results are given by the dashed lines. High-resolution XPS-spectra showcasing the change due to annealing through the **(c)** carbon 1s spectra, **(d)** the oxygen 1s spectra and **(e)** the platinum 4f spectra.

before and after annealing revealed a clear increase in crystallinity, corresponding to a decline in particle size.

Raman spectroscopy was performed to investigate the structure and electronic state of the carbon support structure in the thin-film. The Raman spectra in Fig. 4b shows results predominantly related to the Vulcan XC-72 support and minor contributions from the PTFE. This can also be seen from comparing reference spectra of the other carbon sources in the thin-film (PTFE and Nafion resin) [48,49]. This is also shown by comparing XRD and Raman spectra for electrodes annealed at 500°C and 600°C, as Raman spectra does not change notably between these temperatures despite the absence of a PTFE peak (18.1°) for the 600°C electrode shown in XRD spectra (Fig. S11).

Comparison of the D* band before and after annealing in Fig. 4b shows a greater band width, indicating an increase in disorder in the sp^3 phases typically found in the aliphatic moieties in the carbon support due to the heating process [24,26]. Conversely and by the same logic, the rather notable D" band indicates increased order in the planes in-between the basic structural unit of the polyaromatic layers illustrated in Fig. S14d [24,26,50]. The D and G band decreased after annealing, where the intensity decreased while the width increased. This indicates greater disorder in the edge-adjacent carbon atoms and the in-plane sp^2-bonded carbon atoms respectively [24,25].

All these findings correlate with established temperature-based effects [25] resulting from an increase in the size of the circular carbon black nanoparticles. This can also be determined utilising Eq. (1), where λ corresponds to the wavelength of the laser in nm.

$$L_a = 2.4 \times 10^{-10} \lambda^4 \left(\frac{I_D}{I_G}\right)^{-1} \quad (1)$$

The inverse correlation between the in-plane crystallite size and I_D/I_G ratio shows that the in-plane size increases after annealing while the I_D/I_G ratio decreases as shown in Fig. 4b and in literature [25,26]. The ratio of the intensity (I_D/I_G) is employed to determine relative disorder originating from structural defects in the carbon graphite. Relative to the unheated Pt/C cathode, the I_D/I_G ratio decreased after heating as shown in Fig. 4b indicating a decline in graphitisation.

To determine the oxidation state of the principal elements in the thin-film after annealing, core-level XPS spectra were gathered. XPS results for the cathode shows several distinct peaks before and after heat-treatment as shown in the survey spectra in Fig. S15a. The C 1s spectra for both pristine and annealed cathodes shown in Fig. 4c were deconvoluted to show the sp^3 C–C bond at 284.86 eV and 284.76 eV, the C–O bond at 285.76 eV and 285.66 eV, the C=O bond at 287.11 eV and 287.31 eV, the C–F bond at 289.66 eV and 290.01 eV, the C–F_2 bond at 292.36 and 292.41 eV and the C–F_3 bond at 293.11 eV and 293.16 eV. The C–C bond can be found in all parts of the thin-film, specifically the graphitic carbon in the support of the Pt/C catalyst, the Nafion perfluorinated resin solution (NPRS) and in the PTFE. The C–O bond is primarily affiliated with the carbon support of the catalyst, but also the NPRS. The carbon support is the only contributor to the C=O bond. The C–F and C–F_3 bond are solely from the NPRS, while both NPRS and most importantly PTFE contribute to the C–F_2 bond.

Evidently. there is a general increment in some the binding energies related to the Nafion resin (C–F, C–F_2 and C–F_3) indicating an increased oxidation state, where most notably the binding energy of the C–F bond experiences a 0.35 eV increment. The C–F bond is integral in the largest part of the structurally repeating unit in NPRS (by mass and volume) in addition to being the anchoring point for the branch ending in the sulphonic group (-SO_3^-) responsible for cationic conductivity [51]. This would indicate degradation of NPRS through temperature induced chain scission. Literature has reported similar effects which have been

attributed to an increased chemical shift of the C–F_2 bond [43]. That report was not able to separate the peaks of C–F and C–F_2, hence the aforementioned chain scission of C–F appears likely. The notable change in the shape of the C 1s spectra is quantified in Tab. S1 showing the change in C 1s spectra at each step. The decline in fluorocarbon bonds is affiliated with the oxidation of NPRS after annealing, which is also seen as an increase in the peak position of the F 1s peak. A break in C–F_2 bonds would result in a greater number of C–C bonds, thus explaining the decline in fluorocarbon bonds and an increase in the latter [39,52].

The O 1s spectra shown in Fig. 4d where the deconvolution shows several contributors, namely a small contribution from the Pt-O bond at 529.96 eV and 530.76 eV, bonds related to organics at 532.66 eV and 533.01 eV and adsorbed water at 535.66 eV. The marginal contribution from metal oxides increased after heat treatment in line with what would be expected. The organics arise from the aromatic C–O–C bond in the Vulcan XC-72 carbon support from the Pt/C and the C–O bond from the Nafion perfluorinated resin solution monomer. No clear contributions from adsorbed water were found annealing, exhibiting how the annealing has aided in removing inactive contaminants. Generally, the O 1s spectra was stronger after heating, in line with the increased degree of oxidation initially seen though the chemical shift in the C 1s spectra. The Pt 4f spectra exhibited in Fig. 4e display the characteristic twin peaks originating from the 4f orbitals, namely $4f_{7/2}$ at 71.70 eV and 71.71 eV, and $4f_{5/2}$ at 75.00 eV and 75.16 eV. The peaks were deconvoluted to show the platinum was predominantly metallic, with small contributions from the Pt-O bond. This small contribution matched the small metal-oxygen bond in the oxygen 1s spectra in Fig. 4d. The 4f-spectrum of Pt was greatly enhanced after heat treatment as seen by the increased signal strength in peaks visibility, which is in line with the increase in crystallinity seen in XRD spectra in Fig. 4a. This indicates a fair improvement in surface-adjacent catalyst which should yield an improvement in reaction kinetics.

The $NiFe_2O_4$ anode XPS spectra displayed several characteristic peaks as shown in the survey spectra in Fig. S15a. Both the iron and nickel 2p spectra were notably affected by the large quantity of fluorine in the thin films (originating from the PTFE and Nafion perfluorinated resin solution). The F KLL Auger peaks and the F 1s relaxation overshadowed these regions of the XPS spectra as shown in Fig. S16, thus the XPS-analysis relied upon the iron and nickel 3p spectra. Fig. S17a-S17b displays the XPS spectra affiliated with the O 1s, Fe 3p and Ni 3p spectra from the pristine anode. The O 1s spectra from the pristine $NiFe_2O_4$ anode in Fig. S17a was of sufficient quality, thus enabling the metal-oxide contribution to be deconvoluted to two separate contributions originating from the spinel catalyst at 529.30 and 529.90 eV. These were affiliated with the Ni-O_x and the Fe-O_x bonds respectively. The dominant contribution from the organics were singled out at 532.60 eV, succeeded by a dual contribution from adsorbed water at 535.15 and 536.80 eV. The Fe 3p spectra in Fig. S17b had two primary components, at 55.80 and 56.70 affiliated with the oxidation states of +3 with a smaller contribution of +4 respectively [53,54]. The Ni 3p also in Fig. S17b comprised two contributions at 67.60 and 72.20 eV related to the oxidation states of 2+ and 3+ [55,56], where these oxidation states fit the theoretical oxidation numbers of a $NiFe_2O_4$ spinel.

3.2. Electrochemical

These results were produced following the experimental protocol detailed under "Electrochemical characterisation".

3.2.1. Three-electrode measurements

The effect of annealing the electrodes is immediately seen in Fig. 5 where the LSV results in Fig. 5a show a fair performance increment. The mean current for annealed electrodes increased by 40.4% relative to the untreated version, where this improvement is ascribed to a lower series resistance, and improved HER kinetics as indicated in spectroscopic results. This will also be shown based off electrochemical evidence.

Fig. 5 b shows how the Tafel slope declines after annealing, indicating an improved HER pathway. The Tafel slope of the untreated

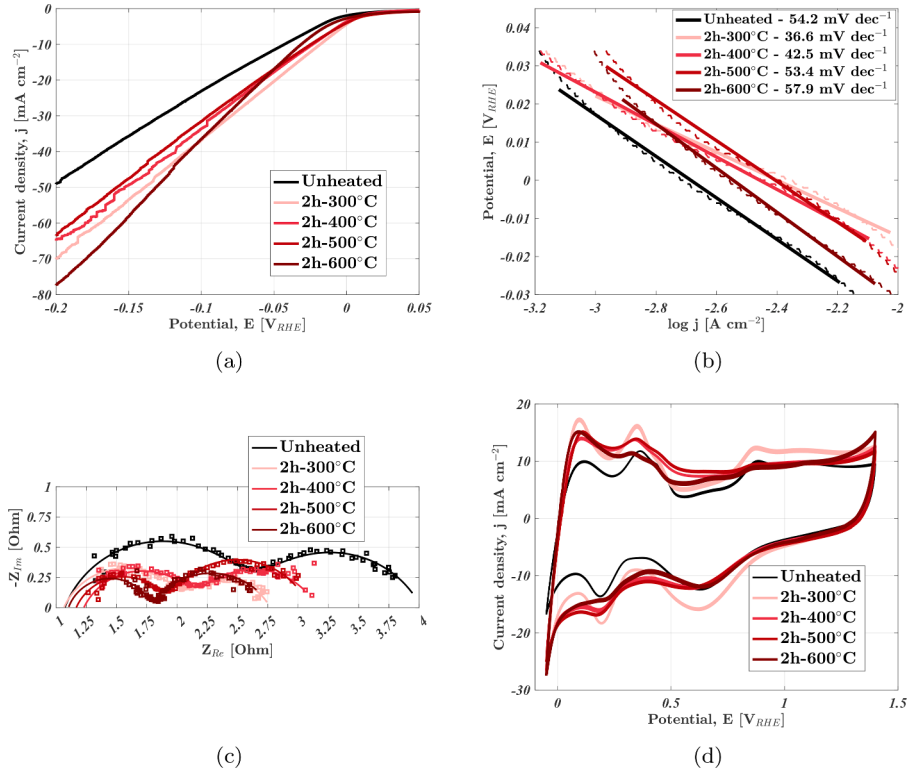

Fig. 5. Three-electrode measurements of Pt-PTFE cathodes annealed for 2 h at various temperatures featuring **(a)** LSV curves, **(b)** Tafel slopes, **(c)** fitted EIS spectra polarised at -100 mV_{RHE} and **(d)** CV curves (v= 100 mV s^{-1}). All measurements are carried out in 1.0 M KOH at 25°C.

electrode implies that the HER proceeds through a combination of the Volmer-Tafel and the Volmer-Heyrovsky pathways, with emphasis on the former [6]. The rate determining step (RDS) was predominantly the Heyrovsky reaction, with some influence of the Volmer reaction. Upon annealing, the Tafel slope drops significantly, and then increases with increasing annealing temperature. Annealing temperatures up to 400°C yield electrodes which proceed exclusively through the Volmer-Heyrovsky pathway as shown by slopes close to 40 mV dec^{-1}. Further increments in temperature result in slopes largely like the unheated electrode.

The hydrophobicity added by PTFE improved stability and bubble detachment, however at the cost of impeding charge transportation due to its insulating qualities [10]. These effects are noticeable in Fig. 5a, where the unheated and 2h-600°C curves represent the extremities of PTFE-effects, namely full effect and no PTFE effect. LSV-curves associated with annealing temperatures below 600°C show some effects of mass transportation issues, which is affiliated with intermediate stages between full and no PTFE-effect. These adverse effects were ameliorated by a rest period in the KOH electrolyte as will be shown later through two-electrode measurements.

The fitted EIS spectra polarised at 100 mV_{RHE} in Fig. 5c has similar trends, as the annealed electrodes clearly have lower charge transfer resistance. The second semicircle attributed to mass transport also declines notably due to annealing, and both facets continue to decline as temperature is increased. This correlates with the trends seen in SEM/EDS and XRD, where the degree of PTFE and thus hydrophobicity declines for temperatures $\geq$ 500°C.

CV scans for the annealed electrodes in Fig. 5d show a marked improvement in electrochemical activity relative to the unheated. For the 2h-300°C electrode, all characteristics appear enhanced. This effect gradually declines as the annealing temperature is increased, where the second hydrogen adsorption peak around 0.35 V_{RHE} is more prominently affected than the first.

The first and second hydrogen adsorption peaks around 0.096 and 0.35 V_{RHE} denote weak and strong hydrogen adsorption respectively [30,33], thereby indicating that increasing the annealing temperature results in a greater proclivity for weak hydrogen adsorption. This affirms the evolution of Tafel slopes with annealing temperature, as the Heyrovsky reaction requires hydrogen to stay adsorbed long enough to react with a nearby water molecule, and the likelihood of this declines as the adsorption strength declines thus increasing the Tafel slope and decreasing the rate of reaction. The electrochemically active surface area (ECSA) shown in Fig. S18a, shows a clear increase in ECSA which peaks for 400–500°C before declining at 600°C. This correlates with the SEM trends in Fig. 2, where the thin-film persists from 300-500°C before undergoing pyrolysis at 600°C. ECSA-normalised LSV curves in Fig. S18b show that annealing increases the ECSA significantly more so than it does the intrinsic activity of the electrodes.

The effect of annealing the PTFE-$NiFe_2O_4$ anode is shown in Fig. S19, where there is a small increment in performance after annealing as shown by the LSV curves in Fig. S19a. The unheated and annealed samples required 374.6 and 356.4 mV overpotential to reach 10 mA cm^{-2} relative to the OER lower heating value, similar to previously reported values [57,58] for such anodes. The pristine and 2h-400°C electrode yielded similar Tafel slopes of 42.8 and 41.3 mV dec^{-1} and similar double layers of as shown in Fig. S19b and S19c [59]. Exchange current densities were estimated to 1.88 and 2.49 $\times$ 10^{-8} mA cm^{-2} for pristine and annealed samples. Cyclic voltammograms in Fig. S19d indicate an earlier onset for the OER and increased influence of the oxidising peak around 1.0 V_{RHE} which was attributed to the chemical transformation/ageing of α-$Ni(OH)_2$ to β-$Ni(OH)_2$ as shown in Eq. (2) [60,61].

$$\alpha - Ni(OH)_2 \longrightarrow \beta - Ni(OH)_2 \quad (2)$$

Moreover, the same CVs show the OER current doubles at 1.60 V_{RHE} after annealing, thus revealing a fair improvement in kinetics after heat treatment. Spectra of EIS at 1.60 V_{RHE} in Fig. S19e show a clear reduction in charge-transfer resistance for the annealed anode, thereby affirming the reduced charge transfer resistance associated with increased catalytic activity displayed in LSV- and CV-curves in Fig. S19a and S19d.

3.2.2. Two-electrode measurements: Performance

The performance of the annealed electrodes was evaluated in a single-cell AEMWE to ascertain their performance under realistic conditions. The LSV performance of the cathodes annealed for 2 h is shown in Fig. 6, and the results from the 3- and 4-hour series are featured in Fig. S20-S23. The 2h performance generally improves over time as exhibited in Fig. 6, where the rest period resulted in a modest increment, while kinetic conditioning through CP produced a more substantial improvement of performance. The augmented performance after repose originates from the electrolyte diffusing into cracks and crevices of the electrodes. This increases the electrical contact, ameliorates mass transportation issues and augments the electrochemically active surface area. EIS analysis correlates this with improvement in series resistance and increments in the double layer region which signifies a greater electrochemically active surface area. This accounts for the similarity between the iR-corrected LSV curves before and after rest. Moreover, this effect declined with temperature, as the hydrophobicity induced by the PTFE was greatly reduced for cathodes annealed at 600°C, thereby decreasing equilibration time. This agrees with results from the three-electrode measurements.

The uncorrected LSV performance of the cell configuration employing the cathodes annealed at 2h-500°C and 2h-600°C greatly surpassed the performance of the untreated reference nickel foam configuration. The uncorrected performance of the reference surpassed the performance of the the 2h-300°C and 2h-400°C cathodes, solely due to its comparatively low series resistance as seen by comparing the EIS spectra in Fig. 7a–f with that in S24b-S24d. Evaluation of the iR-corrected LSV curves shows predictably enough that the reference performance is exceeded by all cell configurations. Comparing the iR-corrected performances after CP at 1.80 V yields current densities of 119, 301, 233, 738 and 365 mA cm^{-2} for the reference, the 2h-300°C, the 2h-400°C, the 2h-500°C and the 2h-600°C cell configurations respectively.

The temperature at which the greatest activity was registered ($T_{act.,\ max}$) was 500°C for the 2 h series, which produced a current density of 1000 mA cm^{-2} at 1.86 V with iR-correction. The penultimate performance 1000 mA cm^{-2} at 2.06 V with iR correction, recorded with the 2h-600°C cathode. Both these curves had similar series resistances, which showcases the importance of a low charge transfer resistance which amounted to a 200 mV reduction in overpotentials at 1000 mA cm^{-2}. Both of these performances were recorded after kinetic conditioning, exhibiting that while degradation rates were registered during the CP (as shown in Tab. S2), the cell performances still improved afterwards. Thus, the kinetic conditioning serves as an additional activation procedure. The current density measured at 2.0 V increased by 11.4, 12.2 and 16.9% on average after kinetic conditioning for the electrodes annealed for 2h, 3h and 4h respectively.

Impedance results from the same configurations follow the same storyline while simultaneously unveiling the distribution of the resistances. Nyquist plots in Fig. 7 show the impedance spectra were fitted to an equivalent circuit with a standard circuit configuration for full water electrolysis cells, namely $R_s \| R_{ct,\ 1}\text{-}CPE_1 \| R_{ct,\ 2}\text{-}CPE_2$ [62]. A decline in series resistance as the heating temperature increases is clear and elaborates the sudden performance increment for the 2h-500°C and 2h-600°C. Here, the series resistance was reduced by approximately 75% relative to the configuration with the 2h-300°C sample. The R_{ct} of the 2h-500°C cell was approximately 39% lower than the 2h-600°C cell after conditioning which amounted to a 200 mV decline in overpotential and the total impedance was 24.5% lower at 1.70V. However, the

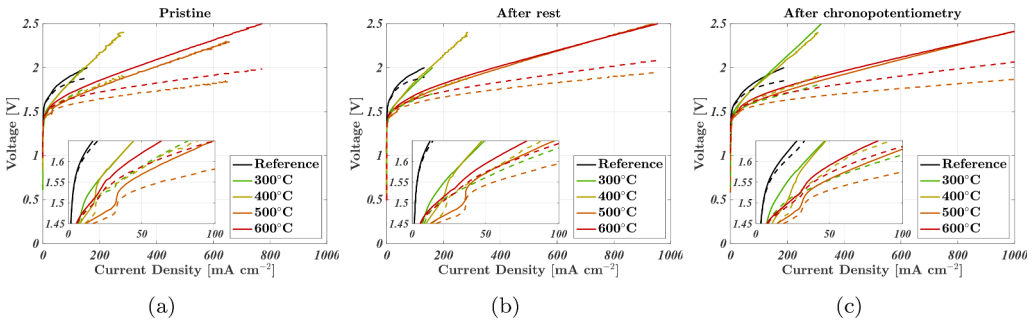

Fig. 6. LSV measured in **(a)** the pristine state, the **(b)** after rest state and **(c)** the state after kinetic conditioning through CP for cell configurations utilising cathodes annealed for 2 h at 300°C, 400°C, 500°C and 600°C compared against the untreated nickel foam reference. The dashed lines represent the iR-corrected curves determined as specified in the experimental section. All measurements were executed in 1.0 M KOH at 50°C.

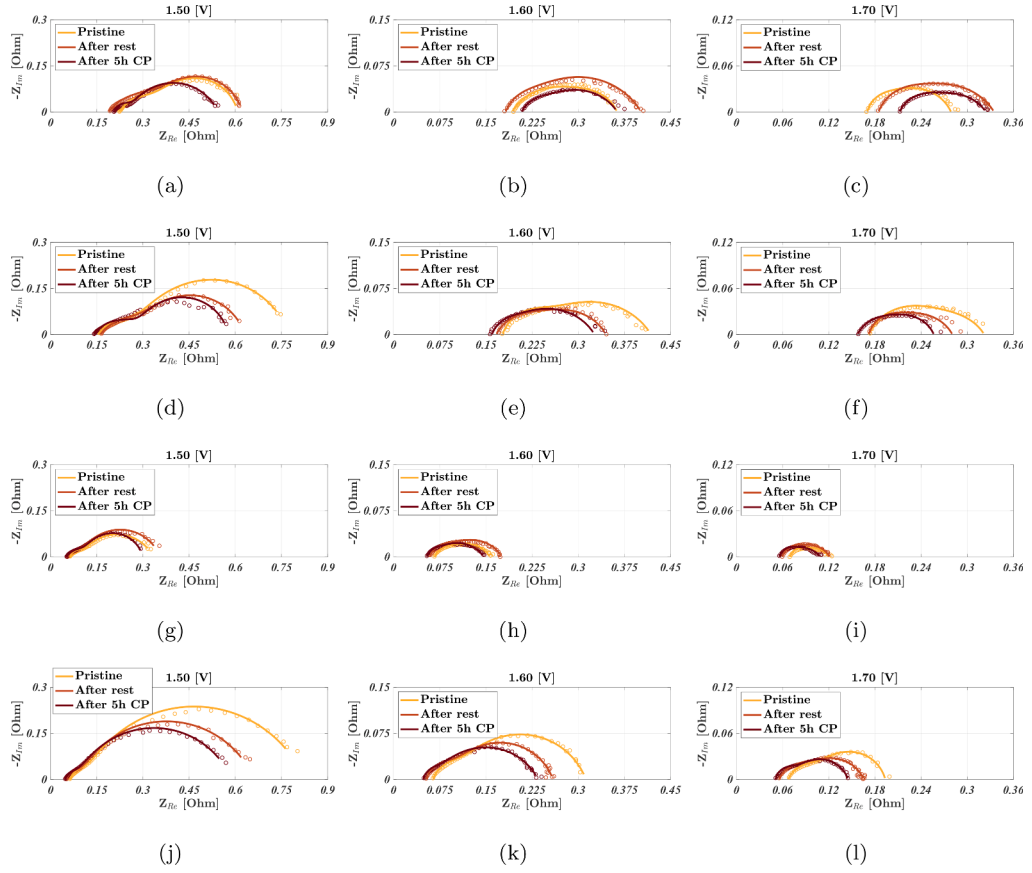

Fig. 7. Polarised EIS spectra from cell configurations employing a cathode annealed for 2 h at 300°C (**(a)-(c)**), 400°C (**(d)-(f)**), 500°C (**(g)-(i)**) and 600°C (**(j)-(l)**). The plots show the fitted impedance spectra of the system polarised at 1.50 V, 1.60 V and 1.70 V measured in a pristine state, the after rest state and the state after CP.

resulting current density shows negligible difference at voltages above 1.70 V, thereby illustrating that catalytic improvements will be limited by the series resistance under realistic operating voltages around 2.0 V.

The AEMWE is assumed to be under kinetic control at 50 mA cm^{-2}, which is easily seen in the LSV curves in Fig. 6. As such, the catalytic activity in all cell configurations were assessed by comparing their total cell potentials at 50 mA cm^{-2}, as shown in Fig. 8a. The lowest potentials for the 2h, 3h and 4h series were located at 500°C, 400°C and 300°C respectively. As such, a staircase effect is observed where increasing annealing time reduces the temperature with the greatest activity.

Fig. 8 b shows the combined anodic and cathodic charge transfer resistance R_{ct} and Fig. 8c displays the series resistance R_s measured through polarised EIS at 1.70 V after the five hours of kinetic conditioning through CP. The same staircase effect is seen in Fig. 8b and Fig. 8a, showing that the combined R_{ct} is potentially a driving force behind this trend and affirms the notion that the AEMWEs were under kinetic control at this current density.

Kinetic activity can be estimated through the inverse correlation between the charge transfer resistance R_{ct} and the exchange current density ($\frac{1}{R_{ct,\,1}} = \left(\frac{di_1}{dV}\right)_{i_{net}=0}$) [63]. The cathodic parameter $1/R_{ct,\,1}$ is determined by fitting the open circuit EIS (i_{net}=0) spectra to an equivalent circuit. The evolution of this parameter is shown in Fig. 8d and is generally similar to the combined R_{ct} in Fig. 8b and the general staircase activity trend.

3.2.3. *Two-electrode measurements: Stability*

All AEMWEs were subject to kinetic conditioning to ascertain their stability and change in catalytic performance, which was carried out

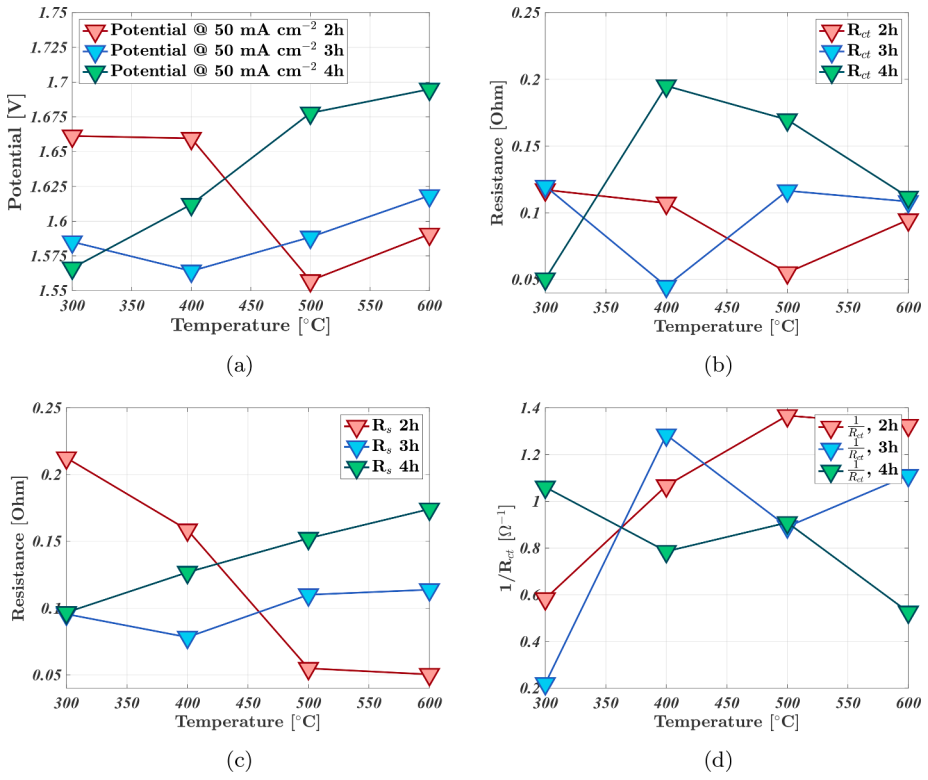

Fig. 8. **(a)** Total potential at 50 mA cm^{-2} as function of temperature for the three heating times after kinetic conditioning through CP. The **(b)** charge transfer resistance R_{ct} and **(c)** the series resistance R_s as a function of temperature determined from EIS spectra polarised at 1.70 V. The inverse HER charge transfer resistance $1/R_{ct1}$ as a function of temperature **(d)**, where R_{ct1} is affiliated with the exchange current density of the HER. The parameter R_{ct1} was determined by fitting open circuit EIS spectra ($i_{net} = 0$) after kinetic conditioning.

through chronopotentiometry (CP) at 50 mA cm^{-2} for 5 h. The low current density was chosen to ensure that the electrolysers were working in a kinetically-controlled region. Fig. 9a displays the CP results of all electrodes from the 2 h series with the nickel foam reference. All cell configurations in Fig. 9a exhibit degradation rates over 1 mV h^{-1}, however these rates would likely decline if the duration was increased. Naturally, the potential exhibited during CP adhered to the same order as seen by comparing it with the activity-temperature plot in Fig. 8a and the original LSV curves in Fig. 6. There is little change in stability as a function of annealing temperature based off the degradation rates in

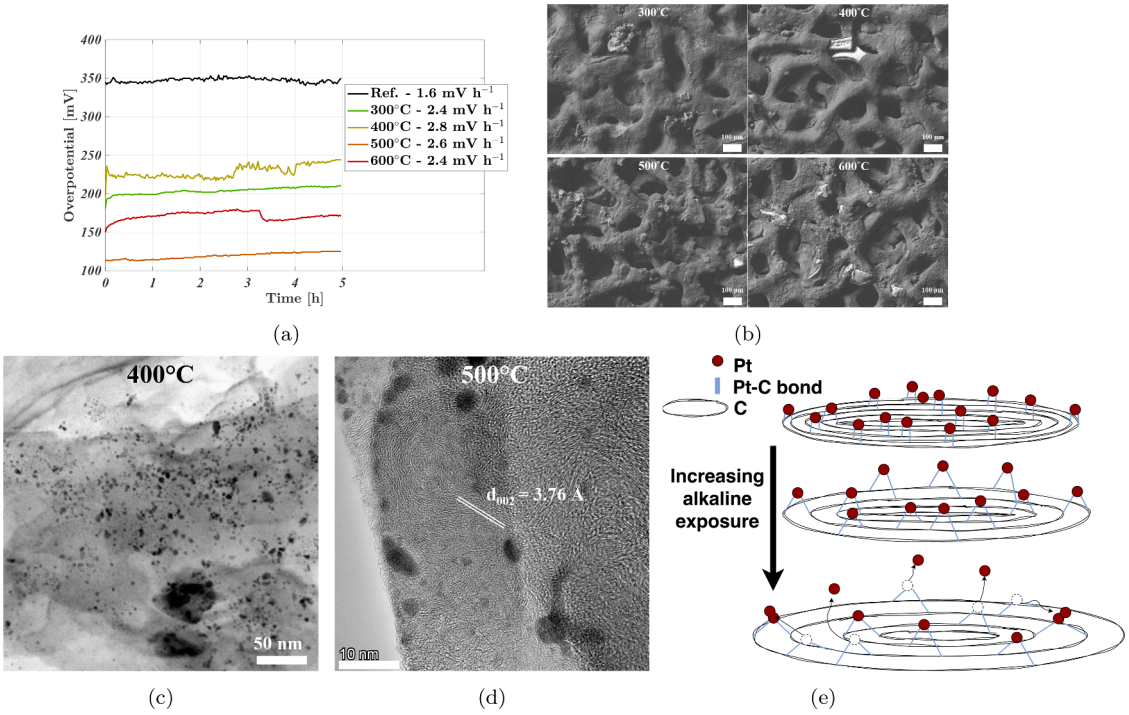

Fig. 9. **(a)** Chronopotentiometry at 50 mA cm^{-2}, 50°C for the cell configurations utilising the cathodes annealed for 2 h at various temperatures and the associated degradation rates. Overpotential is relative to the higher heating value of 1.481 V. **(b)** SEM figures of the PTFE-Pt cathodes annealed for 2 h and **(c)** TEM of the thin film after CP. Detailed surface characteristics are shown in **(d)** through HRTEM. **(e)** Degradation of Pt/C through alkaline exposure, showing Pt detachment/agglomeration from carbon planes due to increased in-plane distance.

Fig. 9a alone, however cathodes annealed at 600°C generally led to greater degradation (Tab. S2). This corresponds to the decreased mechanical integrity due to the loss of PTFE-binder. Additional SEM/EDS, TEM, XRD, Raman spectroscopy and XPS measurements were recorded after these measurements which revealed extensive changes in surface conditions.

Fig. 9 b displays the surfaces of the PTFE-Pt cathodes after electrochemical measurements. Similarly to the pristine condition, the surface morphology changes with temperature, where the surfaces range from smooth and unaltered at 300°C, to uneven and cracked at 600°C. High-temperature samples (500–600°C) displayed a notably greater tendency to produce K_2CO_3 crystals, as determined by the stoichiometry indicated by EDS point analysis and mapping (Fig. S8). This was seen ubiquitously for all high-temperature samples and is very likely related to the electrolyte-surface interaction.

The effect of alkaline electrolysis on the thin film is shown by the post-experimental TEM figure (Fig. 9c). This reveals a greater degree of platinum agglomeration compared against the pristine state shown in Fig. 3e–f. Exposure to the electrochemical environment in the AEMWE results in the thin film showing signs of corrosion where Pt nanoparticles dislodge and agglomerate. HRTEM results in Fig. 9d shows the edge of the carbon particles are frayed compared against the pristine, post-annealed state shown in Fig. 3e–f. Agglomeration effects are also present here, where Pt-nanoparticles appear in small clusters spread with less uniformity. The d_{002} in-plane distance of carbon after CP was measured to 3.76 Å (std = 0.29 Å), thereby revealing an expansion relative to the pristine in-plane distance of 3.39 Å as shown in Fig. S10d. The Pt-Pt d_{111} distance was measured to 2.22 Å (std = 0.14 Å), most similar to the annealed state. Previous reports in literature have alluded to a preference for epitaxial Pt-C anchoring points, between the Pt(111) and C(001) facets [41,64]. Thus, such an increase in d_{002} would also affect the 001-plane and result in substantial strain between these interfaces, and amplify the likelihood of platinum detachment, as illustrated in Fig. 9e.

Fig. 10 a shows XRD patterns of the heat-treated Pt/C cathodes for all temperatures. Diffraction peaks at Bragg angles of 2θ = 17.1°, 18.1°, 24.3°, 30.1°, 31.6°, 36.7°, 39.3° and 40.4° are observed. A variation of ±0.1° in peak position was observed, which originates from height variations during sample mounting and the porous nature of the electrodes. The peaks at 17.1° and 18.2° are related to the Nafion resin and PTFE respectively [16,42]. The large peak width and low intensity of the Nafion peak at 17.1° corresponds to the amorphous nature of the polymer structure, whereas the peaks at 18.1° and 36.7° are from the (100) and (107) planes of PTFE [16,42,44]. Both these peaks were completely missing for electrodes annealed at 600°C where a notable change in both morphology and weight (Fig. S3c) was noted after annealing. This also confirms SEM/EDS results for electrodes annealed at 600°C and the established thermal stability of PTFE [35]. The amorphous peak at 40.5° was attributed to the platinum (111) facet [16, 45]. This peak was not clearly observed for electrodes heated at 600°C, indicating little or no platinum nanoparticles were left after electrochemical measurements. These have likely leached into solution due the lack of the PTFE binder leading to rapid degradation. The peak at 24.3° and the sharp peaks registered between 30-39° were all attributed to various degradation products originating from the interaction between the KOH electrolyte and the carbon surface, namely K_2CO_3 and $KHCO_3$ (JCPDS No. 71-1466 & No. 70-0095) [65,66], which was in line with the results from EDS quantification.

The post-experimental anode XRD spectrum in Fig. S12 shows the same peaks as noted after annealing, thus indicating no additional contaminants. Generally, this spectrum as a whole displays an increase in crystallinity after experiments. The peak affiliated with the (311)-plane undergoes shows a fair increase in crystallinity, which is likely associated with the chemical/electrochemical ageing of the $NiFe_2O_4$ catalyst in an alkaline electrolyte. Notably less influence of the various carbonate species was found on the anode, despite receiving the same treatment as the cathode. Moreover, the peak affiliated with PTFE was still present at 18.1° showing thus showcasing its alkaline stability in the absence of platinum while under oxidising conditions.

The extensive influence of K_2CO_3 in the SEM/EDS and XRD spectra indicates degradation. Previous research shows that a potential weakness lies in the anchoring point(s) between the platinum nanoparticles and the carbon support, where the hydroxide charge carrier reacts with the carbon support ultimately producing carbonate species and

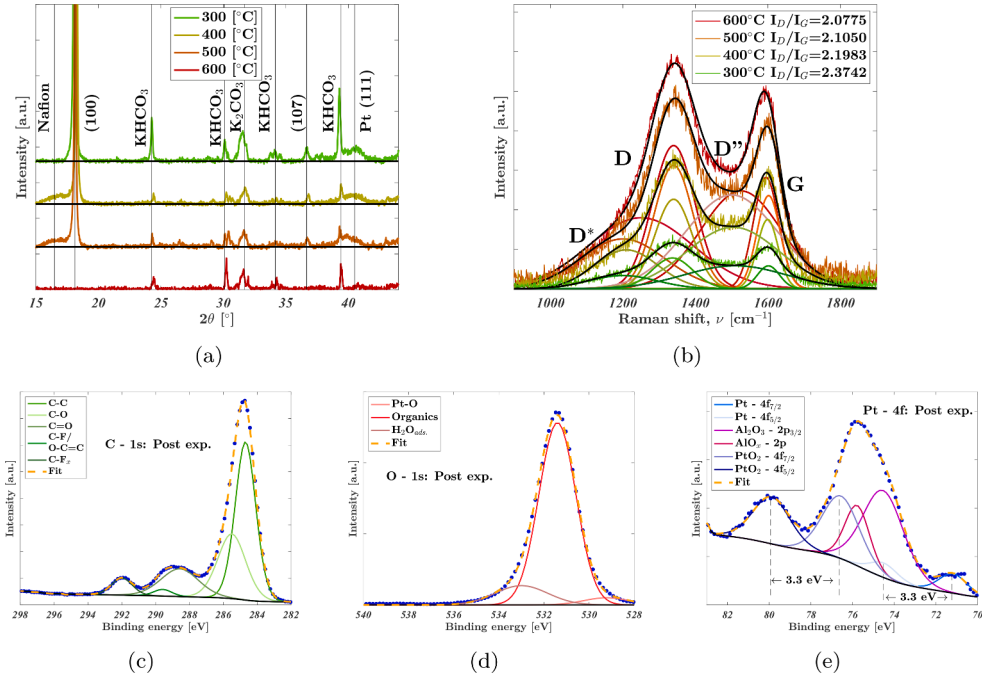

Fig. 10. **(a)** XRD spectra of the 2 h cathodes at several temperatures. **(b)** Raman spectra from the 3 h series shows a representative trend of the electrodes after measurements. **(c)** Post-experimental XPS spectra of originating from the 2h-400°C PTFE-Pt cathode showcasing the carbon 1s spectra, the oxygen 1s spectra and the platinum 4f spectra.

untethered Pt nanoparticles as originally proposed by Lafforgue et al. [67]. Pt was also found to accelerate this process, which corresponds with the complete lack of anodic carbon corrosion. This correlates with the thermodynamic stability of carbon in strong alkaline solutions at potentials above 0.06 V_{RHE} [68]. The increased proclivity to form K_2CO_3 crystals indicates that higher heating temperatures exasperates this degradation mechanism.

Considering the uncertainty associated with the stability of the carbon support, Raman spectra were collected to ascertain its condition. The associated spectra of the cathodes annealed for 3 h (Fig. 10b) were utilised to show how the state of the carbon support varied with temperature, as this set displayed the clearest trends. The same trends are also present in the 2 and 4 h series (Fig. S13), albeit with less clarity. The spectra were fitted utilising the same procedure as that shown for annealed electrodes in Fig. 4b. The evolution of each band with temperature was evaluated by normalising with respect to the baseline signal. The intensity of the D and G bands increase with temperature, indicating increased C–O and C=C stretching and thereby increased molecular polarisability [24,25]. A temperature-related increase of the intensity of the D" band was also revealed, originating from the amorphous sp^2 phase of carbon [24,25].

Moreover, the band width of the D* increases with temperature which indicates rising disorder in the sp^3-rich phases while the width of the D" band decreases indicating increased order in the planes between the planes (Fig. S14d) composed of the polyaromatic BSUs shown in Fig. S14 [24,26,50]. Furthermore, the I_D/I_G ratio decreased continuously with increasing temperature and did not exceed that of the pristine 2h-400°C cathode. The continuous decline in I_D/I_G ratio correlates with temperature-based trends for Vulcan XC-72 [25] and the increased in-plane crystallite size (Eq. (1)). This correlates with the increased d_{002} in-plane distance relative to the pristine value. The trends in the Raman spectra (Fig. 10b) follow the same temperature-based trends from the pre-experimental data, indicating an increase in carbon black particle size. The bonds of a catalyst particle with multiple anchoring points on such an expanding CB surface would likely be affected, as illustrated in Fig. 9e.

Post-experimental XPS spectra reveal the oxidation state of the principal elements of the catalyst thin-film. The survey spectrum in Fig. S15b indicates a few contaminants, where calcium is a common contaminant in the KOH powder utilised to create the KOH electrolyte. The stainless steel fittings are the most likely source of the chromium, which is known to be active under alkaline conditions [27]. The notable presence of zinc is curious, though its sudden appearance after experiments indicates it originated from sample handling, as it cannot originate from the electrolyte as no presence was noted in the anode XPS spectrum (Fig. S15a). The C 1s spectrum in Fig. 10c displayed a great change relative to the pristine and annealed spectra in Fig. 4c. The spectrum was deconvoluted to show the main sp^3 C–C bond at 284.73 eV, the C–O bond at 285.48 eV, the badly oxidised C=O bond at 288.63 eV, the reduced C–F/O–C=C bond at 289.53 eV and finally the severely reduced C–F_x bond at 291.93 eV. Tab. S1 quantifies the fair change in the C 1s spectra, where the clear decline in fluorocarbons indicates corrosion of the PTFE binder. Considering the C=O bond is solely affiliated with the carbon support, its increased binding energy after experiments indicates severe oxidation of the carbon support relative to its annealed state. This correlates with Raman spectra, namely the increased stretching of C–O and rising disorder in sp^3-rich phases (C–C), which indicate carbon corrosion.

The O 1s spectrum displayed a notably greater intensity after experiments (Fig. S15b), thereby producing the sharp peak shown in Fig. 10c. The spectra includes a small, but notably greater contribution from the Pt-O bond at 529.23 eV, the dominant contribution from organics at 531.48 eV and a small addition of adsorbed water at 533.43 eV. The notable contribution from organics increased relative to the annealed state, where this increase is likely related to the formation of compounds such as K_2CO_3 through the degradation of the carbon support. Moreover, the increased size of the metal-oxygen contribution indicates an increase in the platinum oxidation state. This is quite obvious when viewing the Pt 4f spectra in Fig. 10c, where there is a notable difference from the pristine and annealed samples shown in Fig. 4c. The Pt 4f spectrum was deconvoluted to show the traditional 4f-peak split of 3.3 eV yielding the $4f_{7/2}$ and $4f_{5/2}$ peaks of PtO_2 at 76.63 eV and 79.93 eV respectively [69], indicating a significant degree of oxidation. Moreover, lost plasmon peaks of metallic Pt were also located, at 71.23 and 74.53 eV. The peaks attributed to various aluminium oxides come from the aluminium foil utilised for transport of the XPS specimens [70].

The thin-films were briefly exposed to air after electrochemical testing, where CO_2 in the air will react with surface-bound KOH to form K_2CO_3. Post-measurement XPS spectra shown in Fig. 10 revealed notably less platinum, which is supported by EDS measurements (Fig. S3b) showing a lower bulk atomic percentage. The surface-bound Pt-nanoparticles measurable by XPS were notably oxidised, and a greater amount of these nanoparticles were also found in the bulk of the thin film for electrodes annealed at temperatures $\leq$ 500°C as shown by XRD and EDS data. These spectra support the possibility of the degradation pathways suggested by Lafforgue et al. [67].

Despite the clear signs of degradation shown in Fig. 9-10, the utility of PTFE in the thin-film is clear when comparing all the degradation rates in Tab. S2 and the spectroscopic evidence documenting its existence up to 500°C. The catalytic activity of the cathodes increased with temperature, where this was made possible by the binding qualities of PTFE.

Anodic post-experimental XPS results in Fig. S15a & S17c-S17d display the survey spectra, the O 1s and the Fe 3p and Ni 3p spectra respectively. Survey spectra indicate few contaminants, where the calcium originating from the KOH-powder was found here in addition to the cathode. The anodic $NiFe_2O_4$-powder clearly contained traces of manganese and cobalt, which became increasingly present after experiments. The O 1s spectra in Fig. S17c was deconvoluted to show the same contributions as the pristine oxygen 1s spectra in Fig. S17a. It was no longer possible to separate the contributions of iron and nickel in the metal oxide bonds, as only a singular contribution was found at 529.64 eV. The dominant contribution related to the organics (NPRS+PTFE) and the O-H from the catalyst-bound oxygen was located at 531.12 eV, followed by adsorbed water at 532.17 eV. The Fe 3p peak in Fig. S17d is largely unchanged relative to the pristine sample in Fig. S17b, where the same oxidation states are present though with a slight increase. The state of the Ni 3p peaks in Fig. S17d mirror that of the Fe 3p, in showing a slight incline in oxidation state. The average oxidation state of both nickel and iron declined slightly, implying the catalyst was not oxidised. Comparing the relative contributions of iron and nickel in the $NiFe_2O_4$ spinel before and after experiments reveals a clear decline in iron content relative to nickel. This indicates that iron leaches out of the spinel over time, supporting what has been previously reported in literature [71].

4. Conclusion

This paper investigated the annealing conditions of catalyst coated substrates protected by PTFE for Pt/C cathodes and $NiFe_2O_4$ anodes. A barrage of spectroscopic measurements (SEM/EDS, TEM, XRD, Raman spectroscopy and XPS) revealed notable changes in the cathodes after annealing, namely improved morphology and crystallinity. The annealed electrodes were tested in a standard three-electrode cell, where both anode and cathodes exhibited more than 40% improvement in peak current density due to improved OER/HER kinetics and a lower series resistance, thus confirming the spectroscopic prognosis.

Both electrodes were tested in a full AEMWE, where a staircase activity-trend was found as the annealing temperature yielding the

greatest activity declined with increasing annealing time (2h-500°C, 3h-400°C and 4h-300°C). Generally, longer annealing times were not beneficial for cell performance.

The AEMWE performances were recorded at several key points throughout the experimental protocol to quantify the influence of rest, and kinetic conditioning through chronopotentiometry. Cell performance increased after rest, due to electrolyte diffusion decreasing the electrode-AEM contact resistance. Moreover, cell performance generally improved after 5 h of conditioning under kinetic control (50 mA cm^{-2}), with respect to both series and charge transfer resistance. The degree of improvement from kinetic conditioning increased with heating duration, resulting in current densities increasing by 11.4, 12.2 and 16.9% for heating durations of 2h, 3h and 4h respectively measured at 2.0 V.

Electrode stability was evaluated after electrochemical measurements, where annealing temperatures over 500°C resulted in unstable performances. This was related to adverse effects from the annealing process, as temperatures above 500°C compromised the mechanical integrity of the thin-films supported by the PTFE. In-depth surface characterisation revealed degradation from alkaline exposure, where the in-plane distance of the carbon support of the PTFE-Pt cathodes increased, indicating that the onion-like structure of the support expanded during corrosion. Considering the anchoring sites for Pt are hypothesised to be conditional on the similarity between the graphite planes and the Pt-Pt planes through epitaxial growth, this expansion would stretch, weaken, and ultimately break the Pt-C bond, resulting in particle detachment/agglomeration.

The value of utilising PTFE in annealed thin-films has been repeatedly shown, where the conditions of heat treatment have been thoroughly characterised through a barrage of surface-sensitive techniques. This has resulted in both benefits and challenges with respect to AEM water electrolysis. Great benefits have followed kinetic conditioning a AEMWE cell, where the electrode kinetics and most importantly the series resistance was notably improved following this extended activation procedure.

Declaration of Competing Interest

The authors declare that they have no known competing financial interests or personal relationships that could have appeared to influence the work reported in this paper.

Data availability

Data will be made available on request.

Acknowledgments

This project has received funding from the Fuel Cells and Hydrogen 2 Joint Undertaking (now Clean Hydrogen Partnership) under Grant Agreement No 101071111. This Joint Undertaking receives support from the European Union's Horizon 2020 Research and Innovation programme, Hydrogen Europe and Hydrogen Europe Research. "This work was supported by the Swiss State Secretariat for Education, Research and Innovation (SERI) under contract number 101071111."

Supplementary material

Supplementary material associated with this article can be found, in the online version, at 10.1016/j.ceja.2023.100525.

References

[1] C. Li, J.-B. Baek, The promise of hydrogen production from alkaline anion exchange membrane electrolyzers, Nano Energy 87 (2021) 106162.
[2] A. Weiß, A. Siebel, M. Bernt, T.-H. Shen, V. Tileli, H. Gasteiger, Impact of intermittent operation on lifetime and performance of a PEM water electrolyzer, J. Electrochem. Soc. 166 (8) (2019) F487.
[3] T.B. Ferriday, P.H. Middleton, Alkaline fuel cell technology - a review, Int. J. Hydrogen Energy 46 (35) (2021) 18489–18510.
[4] J. Varcoe, P. Atanassov, D. Dekel, A. Herring, M. Hickner, P. Kohl, A. Kucernak, W. Mustain, K. Nijmeijer, K. Scott, T. Xu, L. Zhuang, Anion-exchange membranes in electrochemical energy systems, Energy Environ. Sci. 7 (10) (2014) 3135–3191.
[5] I. Vincent, E.-C. Lee, H.-M. Kim, Comprehensive impedance investigation of low-cost anion exchange membrane electrolysis for large-scale hydrogen production, Sci. Rep. 11 (1) (2021) 1–12.
[6] T.B. Ferriday, P.H. Middleton, M.L. Kolhe, Review of the hydrogen evolution reaction-a basic approach, Energies 14 (24) (2021) 8535.
[7] Y. Park, J. Jeong, Y. Noh, M. Jang, J. Lee, K. Lee, D. Lim, M. Seo, W. Kim, J. Yang, et al., Commercial anion exchange membrane water electrolyzer stack through non-precious metal electrocatalysts, Appl. Catal. B Environ. 292 (2021) 120170.
[8] A. Faid, L. Xie, A. Barnett, F. Seland, D. Kirk, S. Sunde, Effect of anion exchange ionomer content on electrode performance in AEM water electrolysis, Int. J. Hydrogen Energy 45 (53) (2020) 28272–28284.
[9] D. Chen, Y. Park, F. Liu, L. Fang, C. Duan, Hybrid perovskites as oxygen evolution electrocatalysts for high-performance anion exchange membrane water electrolyzers, Chem. Eng. J. (2022) 139105.
[10] M. Cho, H.-Y. Park, S. Choe, S. Yoo, J. Kim, H.-J. Kim, D. Henkensmeier, S. Lee, Y.-E. Sung, H. Park, et al., Factors in electrode fabrication for performance enhancement of anion exchange membrane water electrolysis, J. Power Sources 347 (2017) 283–290.
[11] H. Ito, N. Miyazaki, S. Sugiyama, M. Ishida, Y. Nakamura, S. Iwasaki, Y. Hasegawa, A. Nakano, Investigations on electrode configurations for anion exchange membrane electrolysis, J. Appl. Electrochem. 48 (3) (2018) 305–316.
[12] T. Yu, H.-L. Lin, K.-S. Shen, L.-N. Huang, Y.-C. Chang, G.-B. Jung, J. Huang, Nafion/PTFE composite membranes for fuel cell applications, J. Polym. Res. 11 (3) (2004) 217–224.
[13] L. Wan, Z. Xu, B. Wang, Green preparation of highly alkali-resistant PTFE composite membranes for advanced alkaline water electrolysis, Chem. Eng. J. 426 (2021) 131340.
[14] K. Tomantschger, R. Findlay, M. Hanson, K. Kordesch, S. Srinivasan, Degradation modes of alkaline fuel cells and their components, J. Power Sources 39 (1) (1992) 21–41.
[15] B. Mayerhöfer, F. Speck, M. Hegelheimer, M. Bierling, D. Abbas, D. McLaughlin, S. Cherevko, S. Thiele, R. Peach, Electrochemical-and mechanical stability of catalyst layers in anion exchange membrane water electrolysis, Int. J. Hydrogen Energy 47 (7) (2022) 4304–4314.
[16] G. Avcioglu, B. Ficicilar, A. Bayrakceken, I. Eroglu, High performance PEM fuel cell catalyst layers with hydrophobic channels, Int. J. Hydrogen Energy 40 (24) (2015) 7720–7731.
[17] J. Ohyama, T. Sato, Y. Yamamoto, S. Arai, A. Satsuma, Size specifically high activity of Ru nanoparticles for hydrogen oxidation reaction in alkaline electrolyte, J. Am. Chem. Soc. 135 (21) (2013) 8016–8021.
[18] F. Luo, L. Guo, Y. Xie, J. Xu, W. Cai, K. Qu, Z. Yang, Robust hydrogen evolution reaction activity catalyzed by ultrasmall Rh-Rh_2P nanoparticles, J. Mater. Chem. A 8 (25) (2020) 12378–12384.
[19] X. Zhao, F. Yin, X. He, B. Chen, G. Li, Enhancing hydrogen evolution reaction activity on cobalt oxide in alkaline electrolyte by doping inactive rare-earth metal, Electrochim. Acta 363 (2020) 137230.
[20] M. Jang, J. Yang, J. Jeong, G. Kim, C. Kwon, N. Myung, K. Lee, S. Choi, Promotion effect of modified Ni/C by La-Ce oxide for durable hydrogen evolution reaction, ACS Sustain. Chem. Eng. 9 (37) (2021) 12508–12513.
[21] T. Jawhari, A. Roid, J. Casado, Raman spectroscopic characterization of some commercially available carbon black materials, Carbon 33 (11) (1995) 1561–1565.
[22] A. Sadezky, H. Muckenhuber, H. Grothe, R. Niessner, U. Pöschl, Raman microspectroscopy of soot and related carbonaceous materials: spectral analysis and structural information, Carbon 43 (8) (2005) 1731–1742.
[23] O. Maslova, M. Ammar, G. Guimbretière, J.-N. Rouzaud, P. Simon, Determination of crystallite size in polished graphitized carbon by Raman spectroscopy, Phys. Rev. B 86 (13) (2012) 134205.
[24] J. Ma, A. Habrioux, N. Guignard, N. Alonso-Vante, Functionalizing effect of increasingly graphitic carbon supports on carbon-supported and TiO_2-carbon composite-supported Pt nanoparticles, J. Phys. Chem. C 116 (41) (2012) 21788–21794.
[25] Y. Holade, C. Morais, K. Servat, T. Napporn, K. Kokoh, Enhancing the available specific surface area of carbon supports to boost the electroactivity of nanostructured Pt catalysts, Phys. Chem. Chem. Phys. 16 (46) (2014) 25609–25620.
[26] M. Pawlyta, J.-N. Rouzaud, S. Duber, Raman microspectroscopy characterization of carbon blacks: Spectral analysis and structural information, Carbon 84 (2015) 479–490.
[27] S. Sampathkumar, T. Ferriday, P. Middleton, J. Van Herle, Activation of stainless steel 316l anode for anion exchange membrane water electrolysis, Electrochem. Commun. 146 (2023) 107418.
[28] T. Ferriday, S. Sampathkumar, P. Middleton, J. Van Herle, Investigation of wet-preparation methods of nickel foam for alkaline water electrolysis. Journal of Physics: Conference Series Vol. 2430, IOP Publishing, 2023, p. 012002.
[29] T. Ferriday, S. Sampathkumar, P. Middleton, J. Van Herle, M. Kolhe, How acid washing nickel foam substrates improves the efficiency of the alkaline hydrogen evolution reaction, Energies 16 (5) (2023) 2083.

[30] D. Pletcher, R. Greff, R. Peat, L. Peter, J. Robinson, Instrumental Methods in Electrochemistry, Elsevier, 2001.

[31] J.E. Park, H.E. Bae, M. Karuppannan, K. Oh, O. Kwon, Y.-H. Cho, Y.-E. Sung, Effect of catalyst layer designs for high-performance and durable anion-exchange membrane water electrolysis, J. Ind. Eng. Chem. (2022).

[32] W. Liu, E. Hu, H. Jiang, Y. Xiang, Z. Weng, M. Li, Q. Fan, X. Yu, E. Altman, H. Wang, A highly active and stable hydrogen evolution catalyst based on pyrite-structured cobalt phosphosulfide, Nat. Commun. 7 (1) (2016) 1–9.

[33] A. Zadick, L. Dubau, N. Sergent, G. Berthome, M. Chatenet, Huge instability of Pt/C catalysts in alkaline medium, ACS Catal. 5 (8) (2015) 4819–4824.

[34] S. Poynton, J. Kizewski, R. Slade, J. Varcoe, Novel electrolyte membranes and non-Pt catalysts for low temperature fuel cells, Solid State Ionics 181 (3-4) (2010) 219–222.

[35] L. Chi, Y. Qian, B. Zhang, Z. Zhang, Z. Jiang, Surface engineering and self-cleaning properties of the novel TiO_2/PAA/PTFE ultrafiltration membranes, Appl. Petrochem. Res. 6 (2016) 225–233.

[36] C. Lei, F. Yang, N. Macauley, M. Spinetta, G. Purdy, J. Jankovic, D. Cullen, K. More, Y. Kim, H. Xu, Impact of catalyst ink dispersing solvent on PEM fuel cell performance and durability, J. Electrochem. Soc. 168 (4) (2021) 044517.

[37] T. Kollie, Measurement of the thermal-expansion coefficient of nickel from 300 to 1000 K and determination of the power-law constants near the Curie temperature, Phys. Rev. B 16 (11) (1977) 4872.

[38] L. Lage, P. Delgado, Y. Kawano, Thermal stability and decomposition of Nafion® membranes with different cations - using high-resolution thermogravimetry, J. Therm. Anal. Calorim. 75 (2) (2004) 521–530.

[39] S. Samms, S. Wasmus, R. Savinell, Thermal stability of Nafion® in simulated fuel cell environments, J. Electrochem. Soc. 143 (5) (1996) 1498.

[40] D. Chu, D. Gervasio, M. Razaq, E. Yeager, Infrared reflectance absorption spectroscopy (IRRAS). Study of the thermal stability of perfluorinated sulphonic acid ionomers on Pt, J. Appl. Electrochem. 20 (1) (1990) 157–162.

[41] C. Poidevin, P. Paciok, M. Heggen, A. Auer, High resolution transmission electron microscopy and electronic structure theory investigation of platinum nanoparticles on carbon black, J. Chem. Phys. 150 (4) (2019) 041705.

[42] Y. Lebedev, Y. Korolev, V. Polikarpov, L. Ignat'eva, E. Antipov, X-ray powder diffraction study of polytetrafluoroethylene, Crystallogr. Rep. 55 (4) (2010) 609–614.

[43] C. Huang, K. Tan, J. Lin, K. Tan, XRD and XPS analysis of the degradation of the polymer electrolyte in H_2-O_2 fuel cell, Chem. Phys. Lett. 371 (1-2) (2003) 80–85.

[44] A. Smolyanskii, E. Politova, O. Koshkina, M. Arsentyev, P. Kusch, L. Moskvitin, S. Slesarenko, D. Kiryukhin, L. Trakhtenberg, Structure of polytetrafluoroethylene modified by the combined action of γ-radiation and high temperatures, Polymers 13 (21) (2021) 3678.

[45] S. Hu, M. Tian, E. Ribeiro, G. Duscher, D. Mukherjee, Tandem laser ablation synthesis in solution-galvanic replacement reaction (LASiS-GRR) for the production of PtCo nanoalloys as oxygen reduction electrocatalysts, J. Power Sources 306 (2016) 413–423.

[46] Z. Fang, Z. Hao, Q. Dong, Y. Cui, Bimetallic $NiFe_2O_4$ synthesized via confined carburization in NiFe-MOFs for efficient oxygen evolution reaction, J. Nanopart. Res. 20 (4) (2018) 1–10.

[47] L. Long, Y. Yao, M. Yan, H. Wang, G. Zhang, M. Kong, L. Yang, X. Liao, G. Yin, Z. Huang, Ni_3S_2@polypyrrole composite supported on nickel foam with improved rate capability and cycling durability for asymmetric supercapacitor device applications, J. Mater. Sci. 52 (7) (2017) 3642–3656.

[48] V. Korepanov, E. Kabachkov, S. Baskakov, Y. Shul'ga, Raman spectra of composite aerogels of polytetrafluoroethylene and graphene oxide, Russian J. Phys. Chem. A 94 (11) (2020) 2250–2254.

[49] J.-L. Bribes, M. El Boukari, J. Maillols, Application of Raman spectroscopy to industrial membranes. Part 2–Perfluorosulphonic membrane, J. Raman Spectrosc. 22 (5) (1991) 275–279.

[50] R. Heidenreich, W. Hess, L. Ban, Structure of spherule and layers inferred from electron microscopy and X-ray diffraction, J. Appl. Crystallogr. 1 (1968) 1–19.

[51] A. Trefilov, A. Balan, I. Stamatin, Hybrid Proton-Exchange Membrane Based on Perfluorosulfonated Polymers and Resorcinol-Formaldehyde Hydrogel, Polymers 13 (23) (2021) 4123.

[52] T. Yu, Y. Sha, W.-G. Liu, B. Merinov, P. Shirvanian, W. Goddard III, Mechanism for degradation of Nafion in PEM fuel cells from quantum mechanics calculations, J. Am. Chem. Soc. 133 (49) (2011) 19857–19863.

[53] T. Yamashita, P. Hayes, Effect of curve fitting parameters on quantitative analysis of $Fe_{0.94}O$ and Fe_2O_3 using XPS, J. Electron Spectrosc. Relat. Phenomena 152 (1-2) (2006) 6–11.

[54] A. Punnoose, K. Dodge, J. Beltrán, K. Reddy, N. Franco, J. Chess, J. Eixenberger, C. Barrero, Dopant spin states and magnetism of $Sn_{1-x}Fe_xO_2$ nanoparticles, J. Appl. Phys. 115 (17) (2014) 17B534.

[55] M. Saghayezhian, Z. Wang, H. Guo, Y. Zhu, E. Plummer, J. Zhang, Manipulating the polar mismatch at the $LaNiO_3$/$SrTiO_3$ (111) interface, Phys. Rev. B 95 (16) (2017) 165434.

[56] C. McBean, H. Liu, M. Scofield, L. Li, L. Wang, A. Bernstein, S. Wong, Generalizable, electroless, template-assisted synthesis and electrocatalytic mechanistic understanding of perovskite $LaNiO_3$ nanorods as viable, supportless oxygen evolution reaction catalysts in alkaline media, ACS Appl. Mater. Interfaces 9 (29) (2017) 24634–24648.

[57] M. Silva, R. Raimundo, T. Silva, A. Araújo, D. Macedo, M. Morales, C. Souza, A. Santos, A. Lopes-Moriyama, Morphology-controlled $NiFe_2O_4$ nanostructures: influence of calcination temperature on structural, magnetic and catalytic properties towards OER, J. Electroanal. Chem. (2023) 117277.

[58] G. Liu, K. Wang, X. Gao, D. He, J. Li, Fabrication of mesoporous $NiFe_2O_4$ nanorods as efficient oxygen evolution catalyst for water splitting, Electrochim. Acta 211 (2016) 871–878.

[59] A. Paulraj, Y. Kiros, M. Göthelid, M. Johansson, $NiFeO_x$ as a bifunctional electrocatalyst for oxygen reduction (OR) and evolution (OE) reaction in alkaline media, Catalysts 8 (8) (2018) 328.

[60] Š. Trafela, J. Zavašnik, S. Šturm, K.Ž. Rožman, Controllable voltammetric formation of a structurally disordered $NiOOH/Ni(OH)_2$ redox pair on Ni-nanowire electrodes for enhanced electrocatalytic formaldehyde oxidation, Electrochim. Acta 362 (2020) 137180.

[61] D. Hall, C. Bock, B. MacDougall, The electrochemistry of metallic nickel: oxides, hydroxides, hydrides and alkaline hydrogen evolution, J. Electrochem. Soc. 160 (3) (2013) F235.

[62] S. Siracusano, S. Trocino, N. Briguglio, V. Baglio, A. Aricò, Electrochemical impedance spectroscopy as a diagnostic tool in polymer electrolyte membrane electrolysis, Materials 11 (8) (2018) 1368.

[63] G. Horvai, Relationship between charge transfer resistance and exchange current density of ion transfer at the interface of two immiscible electrolyte solutions, Electroanalysis 3 (7) (1991) 673–675.

[64] E. Willinger, A. Tarasov, R. Blume, A. Rinaldi, O. Timpe, C. Massué, M. Scherzer, J. Noack, R. Schlogl, M. Willinger, Characterization of the platinum–carbon interface for electrochemical applications, ACS Catal. 7 (7) (2017) 4395–4407.

[65] A. Shkatulov, J. Houben, H. Fischer, H. Huinink, Stabilization of K_2CO_3 in vermiculite for thermochemical energy storage, Renew. Energy 150 (2020) 990–1000.

[66] S. Lee, B. Choi, C. Ryu, Y. Ahn, T. Lee, J. Kim, The effect of water on the activation and the co_2 capture capacities of alkali metal-based sorbents, Korean J. Chem. Eng. 23 (2006) 374–379.

[67] C. Lafforgue, F. Maillard, V. Martin, L. Dubau, M. Chatenet, Degradation of carbon-supported platinum-group-metal electrocatalysts in alkaline media studied by in situ fourier transform infrared spectroscopy and identical-location transmission electron microscopy, ACS Catal. 9 (6) (2019) 5613–5622.

[68] M. Pourbaix, Atlas of electrochemical equilibria in aqueous solution, NACE 307 (1974).

[69] J. Hammond, N. Winograd, XPS spectroscopic study of potentiostatic and galvanostatic oxidation of Pt electrodes in H_2SO_4 and $HClO_4$, J. Electroanal. Chem. Interfacial Electrochem. 78 (1) (1977) 55–69.

[70] S.-L. Chang, J. Anderegg, P. Thiel, Surface oxidation of an Al Pd Mn quasicrystal, characterized by X-ray photoelectron spectroscopy, J. Non-Crystalline Solids 195 (1-2) (1996) 95–101.

[71] F. Speck, K. Dettelbach, R. Sherbo, D. Salvatore, A. Huang, C. Berlinguette, On the electrolytic stability of iron-nickel oxides, Chem 2 (4) (2017) 590–597.